

Heterostructured TiO₂ Spheres with Tunable Interiors and Shells toward Improved Packing Density and Pseudocapacitive Sodium Storage

Xin Xu, Bo Chen, Junping Hu, Bowen Sun, Xiaohui Liang, Nan Li, Shengyuan A. Yang, Hua Zhang,* Wei Huang,* and Ting Yu*

Insertion-type anode materials with beneficial micro- and nanostructures are proved to be promising for high-performance electrochemical metal ion storage. In this work, heterostructured TiO₂ spheres with tunable interiors and shells are controllably fabricated through newly proposed programs, resulting in enhanced pseudocapacitive response as well as favorable Na⁺ storage kinetics and performances. In addition, reasonably designed nanosheets in the extrinsic shells are also able to reduce the excess space generated by hierarchical structure, thus improving the packing density of TiO₂ spheres. Lastly, detailed density functional theory calculations with regard to sodium intercalation and diffusion in TiO₂ crystal units are also employed, further proving the significance of the surface-controlled pseudocapacitive Na⁺ storage mechanism. The structure design strategies and experimental results demonstrated in this work are meaningful for electrode material preparation with high rate performance and volume energy density.

abundance, as well as almost unlimited sodium resources on earth, sodium-ion batteries (SIBs or NIBs) are continuously attracting increasing attentions in both of the academic and industrial fields as competitive alternatives for the possible replacement of LIBs.^[2–4] Similar with the performance limit issues in LIB systems, the key challenges for the application and commercialization of NIBs are regarded as the appropriate electrode material selection and design.^[5–7] Among the various candidates for NIB anodes, titanium dioxide (TiO₂) is a promising choice on account of its several superiorities such as structural stability based on intercalation mechanism, safety insurance due to the high working voltage, environmental friendly, and low cost.^[8–13] However, the relatively low specific capacity and inferior rate capability of TiO₂-based anode

Along with the rapid growth of electronic market, the consumption demand of lithium-ion batteries (LIBs) are gradually increased in the past 20 years.^[1] Very recently, owing to the natural limits of lithium resources such as distribution and

materials make them still have the necessity of promotion and optimization. To relieve these natural drawbacks, hollow, hierarchical, and porous architectures are proved to be effective for meliorating the sluggish Na⁺ diffusion kinetics, increasing the

Dr. X. Xu, Prof. W. Huang
Shaanxi Institute of Flexible Electronics (SIFE)
Northwestern Polytechnical University (NPU)
Xi'an 710072, China
E-mail: iamwhuang@nwpu.edu.cn

Dr. X. Xu, B. Sun, X. Liang, N. Li, Prof. T. Yu
Division of Physics and Applied Physics
School of Physical and Mathematical Sciences
Nanyang Technological University
Singapore 637371, Singapore
E-mail: yuting@ntu.edu.sg

Dr. B. Chen, Prof. H. Zhang
Center for Programmable Materials
School of Materials Science and Engineering
Nanyang Technological University
Singapore 639798, Singapore
E-mail: HZhang@ntu.edu.sg


Dr. J. Hu, Prof. S. A. Yang
Research Laboratory for Quantum Materials
Singapore University of Technology and Design
Singapore 487372, Singapore

Dr. J. Hu
School of Science
Nanchang Institute of Technology
Nanchang 330099, China

Prof. S. A. Yang
Center for Quantum Transport and Thermal Energy Science
School of Physics and Technology
Nanjing Normal University
Nanjing 210023, China

Prof. H. Zhang
Department of Chemistry
City University of Hong Kong
Kowloon, Hong Kong, China
E-mail: hua.zhang@cityu.edu.hk

Prof. W. Huang
Key Laboratory of Flexible Electronics (KLOFE) and Institute
of Advanced Materials (IAM)
Nanjing Tech University (NanjingTech)
Nanjing 211800, China

 The ORCID identification number(s) for the author(s) of this article can be found under <https://doi.org/10.1002/adma.201904589>.

DOI: 10.1002/adma.201904589

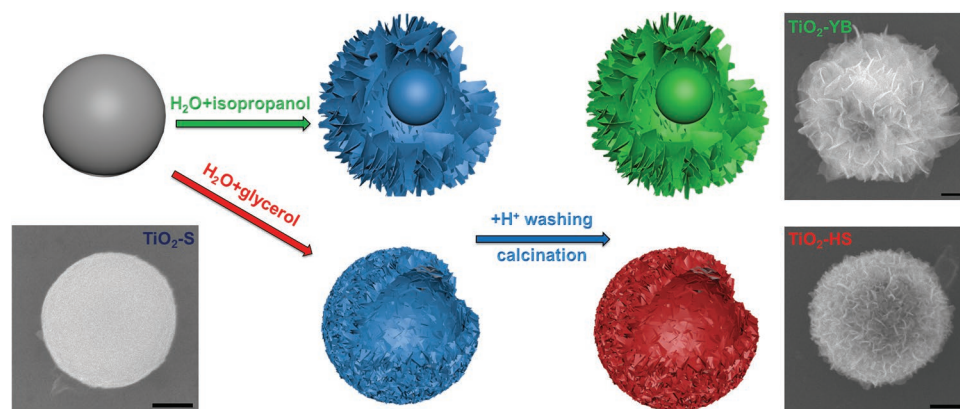


Figure 1. Schematic diagram of the synthesis routes for different TiO_2 spheres and corresponding SEM images of single spheres (scale bars: 200 nm).

active facets for Na^+ storage, as well as strengthening the structural stability of electrodes.^[14–17]

From another point of view, pseudocapacitive charge storage occurred at the surface and/or subsurface of electrode is certified to be significant for the nanostructured crystalline materials, especially under high current densities.^[18–20] This effect is able to enhance both of the rate performance and capacity reversibility of advanced energy storage devices. Compared to the corresponding diffusion-controlled charge storage process which is mainly determined by the inherent crystalline structure and charge storage mechanisms of electrode materials, pseudocapacitive response is much more dependent upon the appropriate electrode material fabrication toward rich extrinsic active sites.^[21,22] Very recently, several previous works present some effective approaches for promoting the pseudocapacitive Li^+/Na^+ storage through structural design and optimization of electrode materials, such as oxygen vacancy creation of metal oxides, size-decreasing, and active facets exposing of nanosheets, interlayer spacing expansion of 2D materials.^[23–27] As far as we know, the relationship between pseudocapacitance and interior/shell adjustments of spherical materials has rarely been involved.

Besides, recent TiO_2 anode related works prove that the combination of different crystalline phases (bronze/anatase) is able to generate beneficial synergistic effect for the enhancement of Li^+/Na^+ intercalation.^[14,28] This kind of heterojunction can not only enhance the structural stability of electrode due to the relatively high crystallization degree, but also maintain the favorable Na^+ storage property associated with the open structure of bronze phase. On the other hand, compared to solid particles, the empty spaces exist in hollow and hierarchical structures are capable of decreasing the material packing densities, thus leading to low volumetric energy densities.^[29–32] Until now, multishelled and asymmetric particles are designed to solve this drawback caused by the “hollow characteristic,” but the extra and wasted space generated by the “hierarchical characteristic” has rarely been noticed to best of our knowledge.

Herein, we employ a simple approach to synthesize a kind of amorphous TiO_2 solid spheres (abbreviated as $\text{TiO}_2\text{-S}$) with uniform size, smooth surface, and good monodispersity (Figure S1, Supporting Information). Afterward, two newly designed programs are introduced to construct TiO_2 hierarchical and hollow

spheres with different core cavities and external shells. Detailed synthesis procedures together with the representative scanning electron microscopy (SEM) images of single TiO_2 sphere are shown in **Figure 1**. According to their morphologies, the TiO_2 yolk-like spheres with bigger nanosheets are named as $\text{TiO}_2\text{-YB}$, and the TiO_2 hollow spheres formed by smaller nanosheets are denoted as $\text{TiO}_2\text{-HS}$. The detailed formation mechanism discussions of these two morphologies are provided in the note of the Supporting Information. Interestingly, the as-prepared $\text{TiO}_2\text{-HS}$ sample possesses higher packing density than that of $\text{TiO}_2\text{-YB}$ due to the size-decreasing of extrinsic nanosheets. As a result, the $\text{TiO}_2\text{-HS}$ sample exhibits the best sodium storage properties among the three anodes, including rate capability, specific capacity as well as cycling stability. In addition, the $\text{TiO}_2\text{-HS}$ anode also displays better electrochemical performances than many other previously reported TiO_2 -based structures. To deeply discuss these facts, detailed Na^+ storage kinetics investigations of the three TiO_2 anodes are also employed, proving the significant connections between high rate Na^+ storage property and pseudocapacitive behavior. In addition, related density functional theory (DFT) calculations including both of the anatase and bronze TiO_2 phases are also simulated based on the first principles, further demonstrating the rationality of our structural design and optimization strategies.

Figure 2a–f and **Figure S2** (Supporting Information) show the detailed morphology and structure observation results of the $\text{TiO}_2\text{-YB}$ and $\text{TiO}_2\text{-HS}$ products by transmission electron microscopy (TEM) and SEM facilities. From the low-resolution TEM images, it can be clearly confirmed that $\text{TiO}_2\text{-YB}$ and $\text{TiO}_2\text{-HS}$ possess yolk-like and hollow interiors, respectively (Figure 2a,b,d,e). In addition, both of the TiO_2 samples display uniform spherical shapes as well as diameters based on the SEM images shown in **Figure S2** of the Supporting Information, due to the suitable self-template technique employed in this work. Particularly, **Figure 2c,f** illustrates the typical shell investigations of the two TiO_2 structures by higher resolution TEM images. As a result, the thickness of the $\text{TiO}_2\text{-HS}$ shell is about 150 nm and half of the $\text{TiO}_2\text{-YB}$, and the nanosheet density of $\text{TiO}_2\text{-HS}$ shell is apparent larger than that of $\text{TiO}_2\text{-YB}$. **Figure 2g** shows the typical high-resolution TEM (HRTEM) image of $\text{TiO}_2\text{-HS}$, the (001) plane of bronze phase (0.62 nm) and the (101) plane of anatase phase (0.35 nm) can be identified,

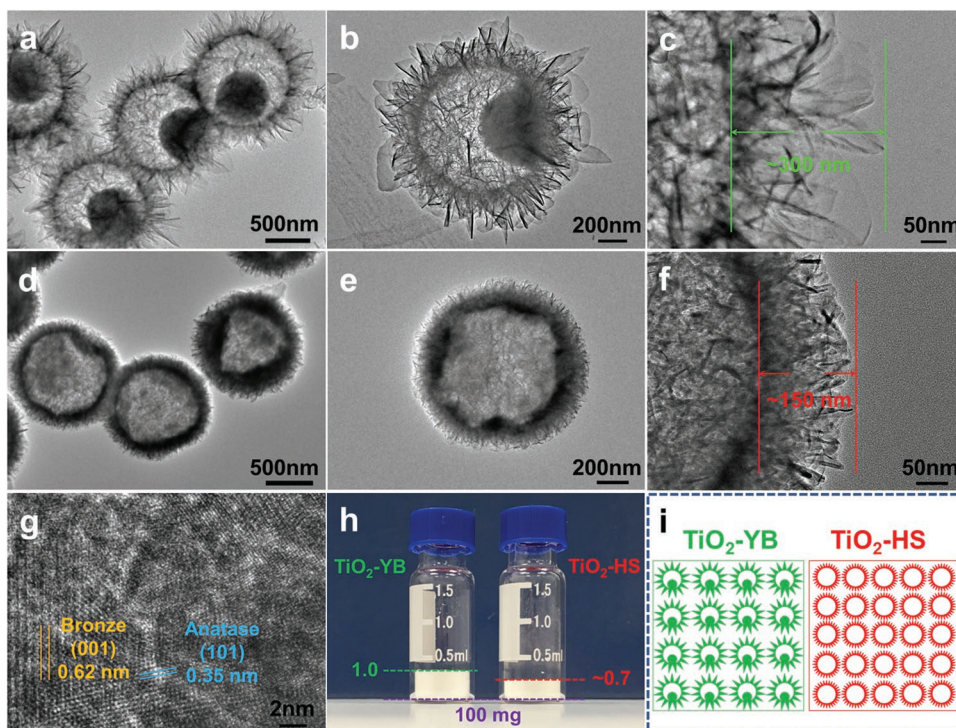


Figure 2. a–f) TEM images of $\text{TiO}_2\text{-YB}$ (a–c) and $\text{TiO}_2\text{-HS}$ (d–f). g) HRTEM image of $\text{TiO}_2\text{-HS}$ showing heterostructure of bronze and anatase phases. h) Digital photograph of tapped $\text{TiO}_2\text{-HS}$ and $\text{TiO}_2\text{-YB}$ samples with the same mass of 100 mg. The $\text{TiO}_2\text{-HS}$ shows a volume ratio of 70% compared to the $\text{TiO}_2\text{-YB}$ (volume ratio is defined as 100%). i) Simplified schematic description of packed $\text{TiO}_2\text{-YB}$ and $\text{TiO}_2\text{-HS}$.

indicating a well formed heterostructure interface. The selected area electron diffraction (SAED) pattern results of heterostructured and anatase $\text{TiO}_2\text{-HS}$ samples are illustrated in Figure S3 of the Supporting Information. As can be seen, the SAED pattern of heterostructured $\text{TiO}_2\text{-HS}$ shows obvious concentric circles, indicating the existence of mixed crystal structures, which are coincident with the previously reported the anatase/bronze TiO_2 samples.^[28] Moreover, the SAED pattern of anatase $\text{TiO}_2\text{-HS}$ calcinated at 500 °C displays clear point matrix, suggesting that the single crystal structure is more dominant. In addition, the element mapping images of $\text{TiO}_2\text{-HS}$ demonstrate that both of the Ti and O are contained in the final product (Figure S4, Supporting Information). Furthermore, the tap density evaluation results of $\text{TiO}_2\text{-HS}$ and $\text{TiO}_2\text{-YB}$ samples are illustrated in Figure 2h. As shown in the digital photograph, $\text{TiO}_2\text{-HS}$ is able to save about 30% excess volume compared to the $\text{TiO}_2\text{-YB}$ under the same weight condition. The improved tap density of hollow and hierarchical structures can not only maintain their favorable characteristics for reversible Li^+/Na^+ storage, but also be promising for high volumetric energy density devices in terms of nano- and micro-scale electrode materials.^[29,33,34] In addition, Figure 2i displays the schematic description of the reason for the previous result: decreasing the size of nanosheets is effective for eliminating the excess space generated by hierarchical structure.

The crystal structures of the three TiO_2 spheres are further detected by X-ray diffraction (XRD), with the patterns illustrated in Figure S5 of the Supporting Information. In Figure S5a of the Supporting Information, the similar and apparent peaks

exhibited by the three TiO_2 samples can be classified as tetragonal anatase-phase (JCPDS 21–1272).^[13] Particularly, the enlarged XRD curves of $\text{TiO}_2\text{-YB}$ and $\text{TiO}_2\text{-HS}$ are made comparisons with the standard peaks of monoclinic bronze-phase (TiO_2 (B), JCPDS 46–1237).^[35] As shown in Figure S5b,c of the Supporting Information, some characteristic peaks at 28.6° (0 0 2), 29.7° (–4 0 1), 29.9° (1 1 1), 43.5° (0 0 3), and 44.5° (–6 0 1) are reflected as weak peaks located at the XRD curves of $\text{TiO}_2\text{-YB}$ and $\text{TiO}_2\text{-HS}$. These facts are also consistent with the previously discussed results based on HRTEM image. To confirm the accurate elemental composition of the final product, X-ray photoelectron spectroscopy is employed and the $\text{TiO}_2\text{-HS}$ sample is tested as a representative, with the related patterns exhibited in Figure S6 of the Supporting Information. The survey spectrum of the $\text{TiO}_2\text{-HS}$ displays its characteristic peaks including Ti 3p, Ti 3s, Ti 2p, O 1s, and Ti 2s located at expected positions (Figure S6a, Supporting Information). Particularly, from Figure S6b of the Supporting Information, the apparent peaks at 458.3 eV (Ti 2p_{3/2}) and 464.3 eV (Ti 2p_{1/2}) represent the existence of Ti^{4+} species.^[28] In addition, another sharp peak located at 529.5 eV in O 1s spectra certifies that O– Ti^{4+} bond is contained in the $\text{TiO}_2\text{-HS}$ sample (Figure S6c, Supporting Information).^[11] Furthermore, N_2 adsorption–desorption isotherms are also employed to investigate the specific surface areas of as-prepared TiO_2 samples (Figure S7, Supporting Information). The calculated results demonstrate that the specific surface areas of $\text{TiO}_2\text{-HS}$ and $\text{TiO}_2\text{-YB}$ (93 and 88 $\text{m}^2 \text{g}^{-1}$) are much larger than that of $\text{TiO}_2\text{-S}$ (31 $\text{m}^2 \text{g}^{-1}$), which are able to provide more sites for electrolyte and solvated Na^+ access

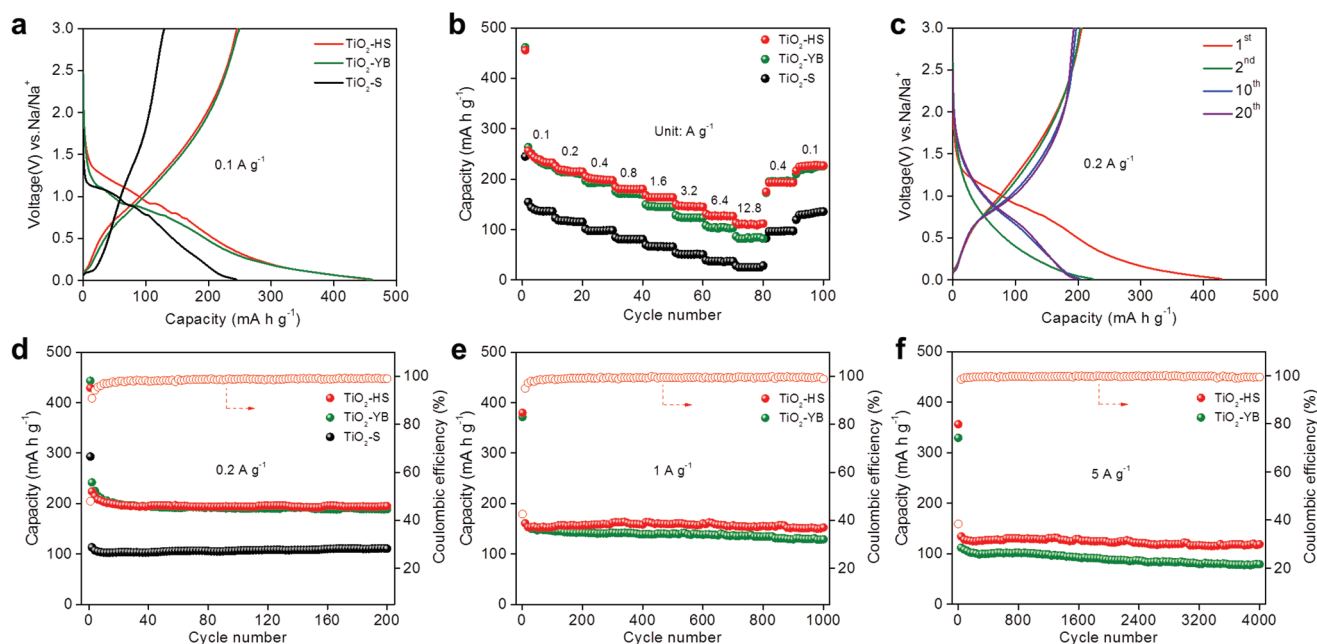


Figure 3. Na⁺ storage properties of different TiO₂ anode materials. a) Initial charge–discharge profiles of TiO₂-HS, TiO₂-YB, and TiO₂-S anodes at 0.1 A g⁻¹, respectively. b) Comparative rate capabilities of the three TiO₂ anodes at stepwisely changed current densities. c) Several charge–discharge profiles of TiO₂-HS anode at 0.2 A g⁻¹. d) Cycling investigations of the three TiO₂ anodes at 0.2 A g⁻¹. e) Cycling properties of TiO₂-HS and TiO₂-YB anodes at 1 A g⁻¹, respectively. f) Long-term cycling performance of TiO₂-HS and TiO₂-YB anodes at 5 A g⁻¹.

(Figure S7a–c, Supporting Information). In addition, pore-size distribution results of the TiO₂ samples are also demonstrated in Figure S7d–f of the Supporting Information. The pore width ranges of TiO₂-S, TiO₂-YB, and TiO₂-HS are mainly 2–5, 4–37, and 4–25 nm, respectively. Thermogravimetric analysis results of the three uncalcined TiO₂ samples are displayed in Figure S8 of the Supporting Information to show the formation processes of final TiO₂ spheres. The weight-loss during the heating process can be ascribed to the conversion of H₂TiO₃ to TiO₂ and the decomposition of involatile organic substances. In view of the previously reported work, TiO₂ samples with amorphous structure exhibit poor rate and cycling performances, which can be ascribed to their unstable architecture for Na⁺ diffusion and storage.^[28] Besides, the involatile organic substances may be unfavorable for the electrolyte, resulting in inferior battery performance. Thus, proper calcination process is significant for improving the quality of electrode materials.

The electrochemical sodium storage behaviors and properties of these TiO₂ samples are investigated via assembled half-cells, with the rate and cycling results shown in **Figure 3**. First, the initial galvanostatic discharge–charge profiles of the electrodes at 0.1 A g⁻¹ are made a contrast in Figure 3a. Clearly, the TiO₂-HS anode shows obvious higher voltage platform during the sodiation process as well as lower polarization, indicating that relatively lower energy barrier for Na⁺ storage and diffusion is generated. Due to the reasonable optimization for the interior and shell of TiO₂ spheres, the TiO₂-HS is able to acquire higher surface area as well as more exposed active crystal facets, which is significant for enhancing the Na⁺ adsorption and transportation processes, and these facts will be simulated by theoretical calculations and discussed later.^[20,24] In addition, the TiO₂-S

electrode displays typical battery-like galvanostatic profiles, indicating the limited surface-controlled charge storage.^[21] Next, rate capability results under progressively increased current densities (from 0.1 to 12.8 A g⁻¹) are revealed in Figure 3b. As can be seen, the specific capacities of TiO₂-HS are similar with that of TiO₂-YB, but much larger than that of TiO₂-S at lower current densities. Furthermore, the TiO₂-HS is able to output obviously larger specific capacities compared to TiO₂-YB during higher rates. As a result, the TiO₂-HS demonstrates a capacity of 112 mAh g⁻¹ at the maximum current density, which is more remarkable compared to many other recently prefabricated pure TiO₂ anodes as well as TiO₂-carbon composites (Figure S9, Supporting Information).^[28,35–40] On the other side, cycling properties of the different TiO₂ anodes at constant currents are also tested in detail. Figure 3c shows the typical discharge–charge voltage profiles of TiO₂-HS electrode at 0.2 A g⁻¹ corresponding to the 1st, 2nd, 10th, and 20th loops. After the first several cycles, the curves illustrate apparent high voltage plateaus and become well overlapped, suggesting much safer sodium storage by avoiding the dendritic growth, as well as favorable capacity reversibility. Notably, there is a substantial difference between the charge–discharge curves of the 2nd and 10th cycles, which is consistent with the previously reported TiO₂ anodes and termed as activation process.^[41,42] Figure 3d demonstrates the cycling properties of the three as-prepared TiO₂ samples at low rate of 0.2 A g⁻¹. Significantly, both of the TiO₂-HS and TiO₂-YB display similar and stable cycling performances, with much larger capacities compared to the TiO₂-S electrode, which can be attributed to the numerous active sites provided by the hollow and hierarchical structures. As a comparison, anatase TiO₂-HS sample is also tested at 0.2 A g⁻¹, which shows lower capacities

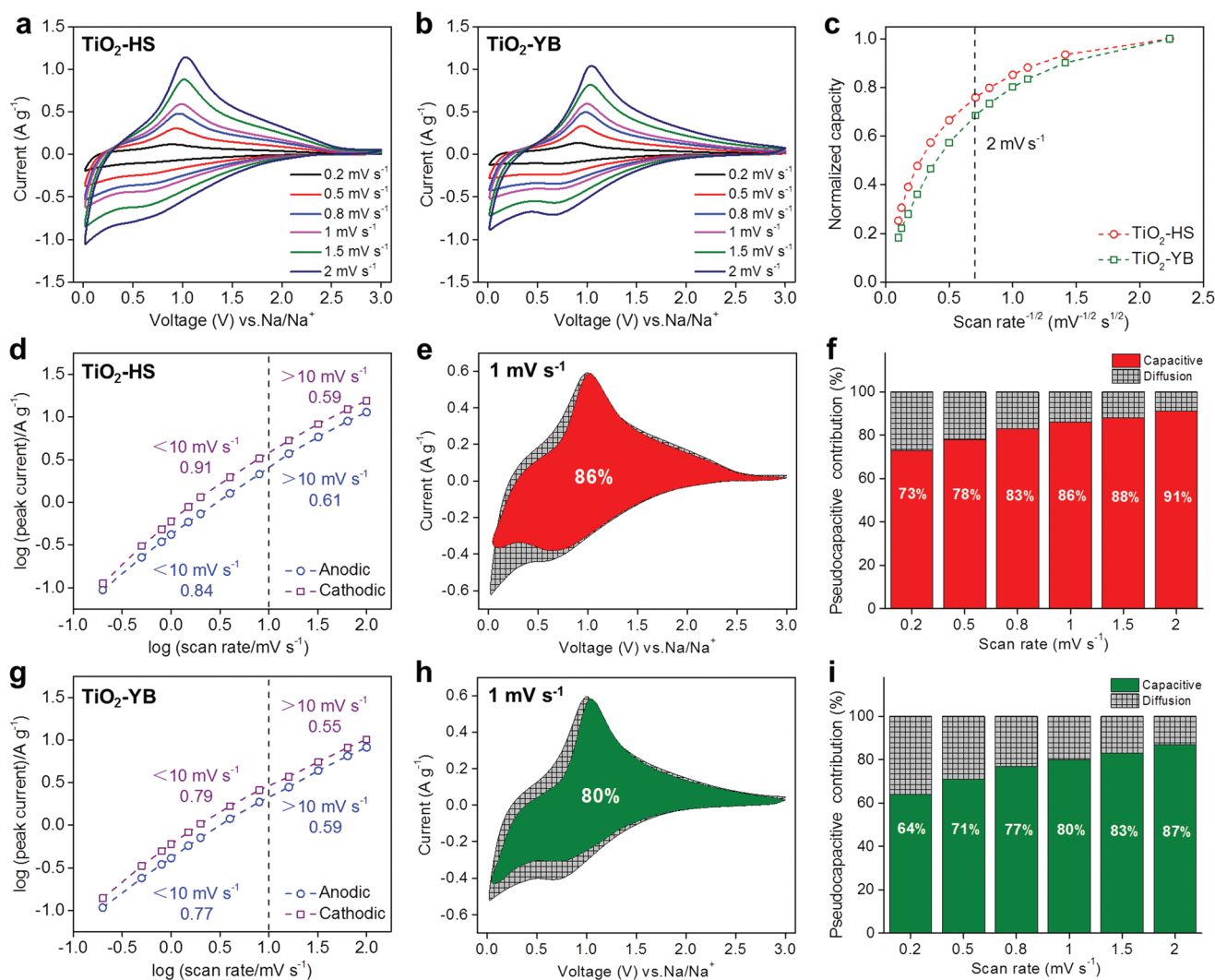


Figure 4. Quantitative analysis of Na^+ storage kinetics for the $\text{TiO}_2\text{-HS}$ and $\text{TiO}_2\text{-YB}$ samples. a,b) CV curves of $\text{TiO}_2\text{-HS}$ (a) and $\text{TiO}_2\text{-YB}$ (b) anodes at 0.2–2 mV s^{-1} , respectively. c) Normalized capacity versus scan rate $^{-1/2}$ plots for both of the $\text{TiO}_2\text{-HS}$ and $\text{TiO}_2\text{-YB}$ anodes. d,g) Logarithm peak current versus logarithm scan rate curves, e,h) separation of capacitive and diffusion controlled currents at 1 mV s^{-1} , and f,i) pseudocapacitive contribution ratio during different sweep rates for the $\text{TiO}_2\text{-HS}$ and $\text{TiO}_2\text{-YB}$ anodes, respectively.

of 162 mAh g^{-1} than that of heterostructured $\text{TiO}_2\text{-HS}$, thus further proving the favorable synergetic effect of bronze and anatase phases (Figure S10, Supporting Information). Furthermore, $\text{TiO}_2\text{-HS}$ and $\text{TiO}_2\text{-YB}$ anodes are selected and tested at higher rate of 1 A g^{-1} and the results are shown in Figure 3e. After the prolonged 1000 cycles, $\text{TiO}_2\text{-HS}$ illustrates more stable capacity retention ability than that of $\text{TiO}_2\text{-YB}$. This is because that more quantity and smaller size of nanosheets are able to reduce the energy barrier of Na^+ diffusion as well as increase the structural stability of the TiO_2 anodes, which will be discussed later. Even after 4000 cycles at 5 A g^{-1} , the $\text{TiO}_2\text{-HS}$ electrode can still deliver a specific capacity of 119 mAh g^{-1} , leading to around 2.8% reversible capacity loss per 1000 cycles, which is still better than that of $\text{TiO}_2\text{-YB}$ sample (Figure 3f). Besides, the initial Coulombic efficiency values of the rate and cycling tests are summarized in Table S2 of the Supporting Information, which are in the range of 35–55%. This phenomenon is

common for metal oxide/sulfide based anodes in the fields of LIBs and NIBs.^[24–29,35–40] The irreversible loss of capacity in these anodes can in some cases be offset by prelithiation/sodiation technologies.^[43,44] The morphologies of three TiO_2 anodes after the repeated sodiation and desodiation processes are also investigated, with the results demonstrated in Figure S11 of the Supporting Information. The well maintained micro- and nanostructures of these TiO_2 spheres intuitively explained their cycling stabilities. Moreover, Nyquist plots of the three TiO_2 electrodes before cycles are also tested with the results shown in Figure S12 of the Supporting Information. Figure S12a,b of the Supporting Information shows the complete and partial curves of the three samples in the frequency range of 0.01–1 000 000 and 0.1–1 000 000 Hz, respectively. To be more accurate, the fitted curves, equivalent circuit models as well as obtained impedance parameters are demonstrated in Figure S12c,d of the Supporting Information. As a result, the charge-transfer

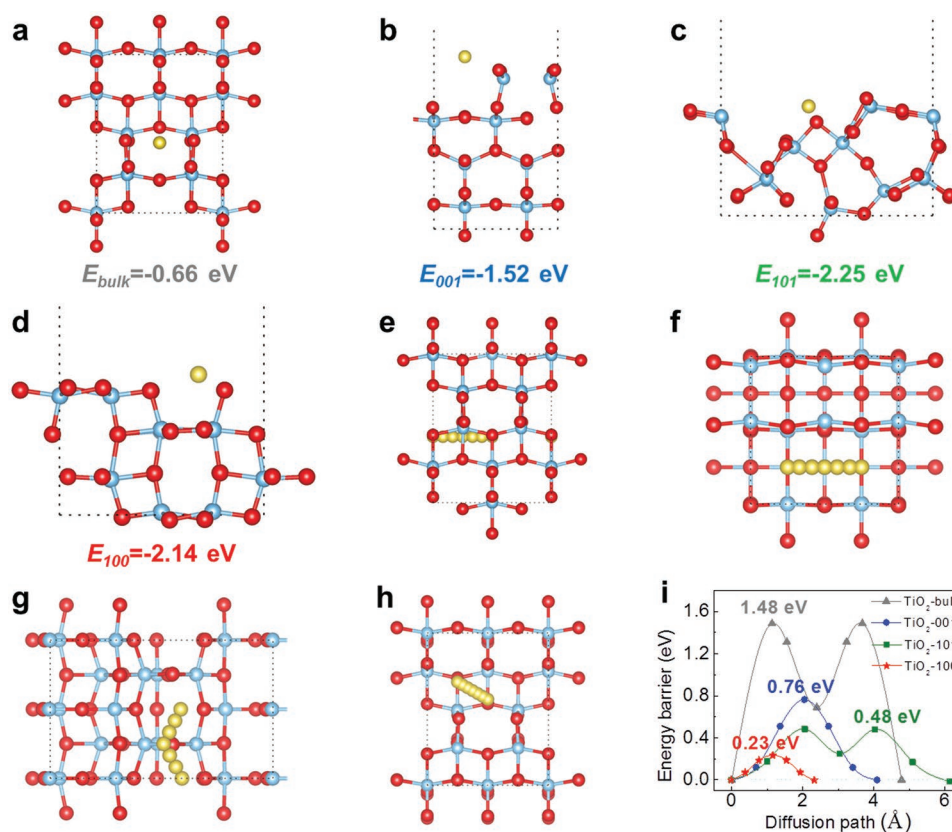


Figure 5. Theoretical calculations of Na storage and diffusion in anatase TiO_2 . a–d) Optimized models of Na adsorption in/on the bulk structure, exposed (001), (010), and (100) facets, respectively. e–h) Na diffusion paths in/on the bulk structure, exposed (001), (010), and (100) facets, respectively. i) Energy barrier-diffusion path profiles of different models.

resistances (R_{ct}) of the TiO_2 -HS, TiO_2 -YB, and TiO_2 -S electrodes show very limited increasing trend, suggesting that the morphology change of TiO_2 spheres possesses relatively small influence on the electroconductivity of whole electrodes.

From the previous morphology and performance evaluations, it is found that the structure change of anode materials possess strong relationship with the capacity and stability of batteries. To analyze this relationship more deeply and accurately, further Na^+ storage kinetics analysis of different TiO_2 samples is conducted based on cyclic voltammetry (CV) profiles. Figure 4a,b and Figure S14 of the Supporting Information display the continuous CV curves (from 0.2 to 100 mV s^{-1}) of TiO_2 -HS and TiO_2 -YB anodes with obvious pseudocapacitive behavior. As can be distinguished, the corresponding anodic and cathodic peaks of the two anodes revealed slight discrepancies, suggesting dissimilar Na^+ storage kinetics. Figure 4c illustrates the relationship between normalized capacities and scan rates ($\nu^{-1/2}$) of the two TiO_2 electrodes. Coincidence with the previous rate performance results, the capacity retention ability of TiO_2 -HS is more outstanding than that of TiO_2 -YB. Furthermore, according to the CV results and power-law equation: $i = a\nu^b$, b values can be calculated to evaluate the Na^+ storage approaches including capacitive- and diffusion-controlled processes.^[19–21] Taking the TiO_2 -HS anode for example, the b values can be calculated as 0.91 and 0.84 for cathodic and anodic peaks when the scan rates are below 10 mV s^{-1} , as well as 0.59 and 0.61

along with the scan rates increased to more than 10 mV s^{-1} , indicating that mixed processes are generated (Figure 4d). In addition, the capacitive-controlled (i_1) and diffusion-dominated (i_2) currents are also able to be divided by another equation of $i = i_1 + i_2 = k_1\nu + k_2\nu^{1/2}$. As illustrated in Figure 4e, at the scan rate of 1 mV s^{-1} , the capacitive-controlled charge storage percentage of TiO_2 -HS anode is around 86%. As a comparison, the calculated b values of TiO_2 -YB (0.79 and 0.77, below 10 mV s^{-1} ; 0.55 and 0.59, above 10 mV s^{-1}) are totally smaller than the corresponding results of TiO_2 -HS, demonstrating that the capacitive-controlled Na^+ storage process of TiO_2 -YB is weaker than that of TiO_2 -HS (Figure 4g). In addition, the capacitive contribution of TiO_2 -YB is about 80% at 1 mV s^{-1} (Figure 4h), as well as the whole calculated results (from 0.2 to 2 mV s^{-1}) are smaller than that of TiO_2 -HS (Figure 4f,i). Furthermore, as expected, the calculated kinetics results of TiO_2 -S are also presented in Figure S15 of the Supporting Information, indicating much stronger diffusion-controlled Na^+ storage mechanism. In one word, these facts prove that the evolution of surface-controlled capacitive behavior generated by morphology change of TiO_2 spheres is the pivotal reason for high rate Na^+ storage.

Based on the former experimental data, sodium storage behaviors and performances of the TiO_2 samples display obvious differences due to the morphology and structure changes. Moreover, increased surface area also means more exposed facets for nanoscale crystal materials. To further

understand these facts, detailed DFT simulations of the Na storage and diffusion based on the first principles are employed. As shown in **Figure 5a–d**, the optimized models of single Na storage in/on anatase TiO₂ crystal units including bulk structure, exposed (001), (101), and (100) facets are established. The corresponding adsorption energies can be calculated as −0.66, −1.52, −2.25, and −2.14 eV, respectively. As for the bronze TiO₂, Na adsorption energies of the bulk structure, exposed (001), (010), and (100) facets are also obtained as −1.71, −0.75, −2.39, and −3.15 eV, respectively (**Figure S16**, Supporting Information). As a comparison, bronze TiO₂ phase is more beneficial for Na storage with relatively lower adsorption energies, which can be attributed to its open crystal framework. In addition, exposed active facets also demonstrate more stable Na storage characteristics compared to the bulk TiO₂, thus certifying the significance of surface capacitive-controlled Na storage process again. In addition, according to the optimized single Na diffusion paths of bulk structure, exposed (001), (101), and (100) facets (**Figure 5e–h**), the calculated energy barriers for each model are 1.48, 0.76, 0.48, and 0.23 eV, respectively, as summarized in **Figure 5i**. These results further prove that exposed facet and surface Na storage is significant for reducing the internal energy consumption as well as increasing structure stability of TiO₂ electrode. The DFT calculation results are well consistent with the previous experimental facts as well as pointing out the more favorable material design route with regard to crystal structure and exposed facets.

In this work, a series of TiO₂ spheres are designed and fabricated toward advanced NIB anodes. Taking advantage of the newly developed synthesis programs, two kinds of TiO₂ spheres with tunable interiors and shells are obtained based on the suitable self-template technique. After calcination, heterostructured TiO₂ spheres with anatase and bronze phases are produced. Interestingly, decreasing the size and increasing the density of nanosheets in the extrinsic shells are able to significantly reduce the extra and wasted space, thus improving the tap density of hierarchical and hollow spheres for future high volumetric energy devices. In addition, the TiO₂-HS possesses the highest surface area among the three TiO₂ spheres, suggesting the most exposed active facets. When tested for reversible sodium storage, TiO₂-HS shows the best electrochemical properties among the three anode materials, including rate capability, specific capacity as well as cycling stability. Moreover, detailed kinetics analysis further confirms the significance of the relationship between pseudocapacitive behavior and rate capability, as well as the suitable structure design. Lastly, DFT calculations are employed to theoretically investigate the Na storage and diffusion in/on different exposed facets and lattice of TiO₂, resulting in solid consistency with the previous experimental facts and conclusions. In summary, the research experiences and results based on TiO₂ are promising for many other electrode materials, toward high-performance electrochemical energy storage devices in the future.

Supporting Information

Supporting Information is available from the Wiley Online Library or from the author.

Acknowledgements

X.X. and B.C. contributed equally to this work. This work was mainly supported by MoE Tier 1 (RG19/17). W.H. thanks the supports by the National Basic Research Program of China-Fundamental Studies of Perovskite Solar Cells (2015CB932200), Natural Science Foundation of Jiangsu Province (BM2012010), Priority Academic Program Development of Jiangsu Higher Education Institutions (YX03001), Ministry of Education of China (IRT1148), Synergetic Innovation Center for Organic Electronics and Information Displays, and the National Natural Science Foundation of China (61136003, 51173081). H.Z. thanks the support from ITC via Hong Kong Branch of National Precious Metals Material Engineering Research Center, and the Start-Up Grant from City University of Hong Kong.

Conflict of Interest

The authors declare no conflict of interest.

Keywords

heterostructures, Na⁺ storage, packing density, pseudocapacitance, TiO₂ spheres

Received: July 17, 2019

Revised: September 16, 2019

Published online: September 30, 2019

- [1] M. Armand, J. M. Tarascon, *Nature* **2008**, 451, 652.
- [2] N. Yabuuchi, K. Kubota, M. Dahbi, S. Komaba, *Chem. Rev.* **2014**, 114, 11636.
- [3] J. Y. Hwang, S. T. Myung, Y. K. Sun, *Chem. Soc. Rev.* **2017**, 46, 3529.
- [4] P. K. Nayak, L. Yang, W. Brehm, P. Adelhelm, *Angew. Chem., Int. Ed.* **2018**, 57, 102.
- [5] M. Lao, Y. Zhang, W. Luo, Q. Yan, W. Sun, S. X. Dou, *Adv. Mater.* **2017**, 29, 1700622.
- [6] H. Hou, X. Qiu, W. Wei, Y. Zhang, X. Ji, *Adv. Energy Mater.* **2017**, 7, 1602898.
- [7] H. Zhang, I. Hasa, S. Passerini, *Adv. Energy Mater.* **2018**, 8, 1702582.
- [8] Q. Xia, Y. Huang, J. Xiao, L. Wang, Z. Lin, W. Li, H. Liu, Q. Gu, H. K. Liu, S. L. Chou, *Angew. Chem., Int. Ed.* **2019**, 58, 4022.
- [9] H. He, D. Huang, W. Pang, D. Sun, Q. Wang, Y. Tang, X. Ji, Z. Guo, H. Wang, *Adv. Mater.* **2018**, 30, 1801013.
- [10] B. Li, B. Xi, Z. Feng, Y. Lin, J. Liu, J. Feng, Y. Qian, S. Xiong, *Adv. Mater.* **2018**, 30, 1705788.
- [11] C. Chen, Y. Wen, X. Hu, X. Ji, M. Yan, L. Mai, P. Hu, B. Shan, Y. Huang, *Nat. Commun.* **2015**, 6, 6929.
- [12] Z. Le, F. Liu, P. Nie, X. Li, X. Liu, Z. Bian, G. Chen, H. B. Wu, Y. Lu, *ACS Nano* **2017**, 11, 2952.
- [13] Y. Zhang, C. Wang, H. Hou, G. Zou, X. Ji, *Adv. Energy Mater.* **2017**, 7, 1600173.
- [14] H. Ren, R. Yu, J. Qi, L. Zhang, Q. Jin, D. Wang, *Adv. Mater.* **2019**, 31, 1805754.
- [15] X. Y. Yu, L. Yu, H. B. Wu, F. X. Ma, X. W. Lou, *Angew. Chem., Int. Ed.* **2015**, 54, 4001.
- [16] B. Y. Guan, L. Yu, J. Li, X. W. Lou, *Sci. Adv.* **2016**, 2, e1501554.
- [17] K. Lan, Y. Liu, W. Zhang, Y. Liu, A. Elzatahry, R. Wang, Y. Xia, D. Al-Dhayan, N. Zheng, D. Zhao, *J. Am. Chem. Soc.* **2018**, 140, 4135.
- [18] J. B. Cook, H. S. Kim, T. C. Lin, C. H. Lai, B. Dunn, S. H. Tolbert, *Adv. Energy Mater.* **2017**, 7, 1601283.

- [19] V. Augustyn, J. Come, M. A. Lowe, J. W. Kim, P. L. Taberna, S. H. Tolbert, H. D. Abruña, P. Simon, B. Dunn, *Nat. Mater.* **2013**, *12*, 518.
- [20] D. Chao, C. Zhu, P. Yang, X. Xia, J. Liu, J. Wang, X. Fan, S. V. Savilov, J. Lin, H. J. Fan, *Nat. Commun.* **2016**, *7*, 12122.
- [21] P. Simon, Y. Gogotsi, B. Dunn, *Science* **2014**, *343*, 1210.
- [22] V. Augustyn, P. Simon, B. Dunn, *Energy Environ. Sci.* **2014**, *7*, 1597.
- [23] H. S. Kim, J. B. Cook, H. Lin, J. S. Ko, S. H. Tolbert, V. Ozolins, B. Dunn, *Nat. Mater.* **2017**, *16*, 454.
- [24] X. Xu, R. Zhao, B. Chen, L. Wu, C. Zou, W. Ai, H. Zhang, W. Huang, T. Yu, *Adv. Mater.* **2019**, *31*, 1900526.
- [25] Y. Xiao, P. F. Wang, Y. X. Yin, Y. F. Zhu, Y. B. Niu, X. D. Zhang, J. Zhang, X. Yu, X. D. Guo, B. H. Zhong, Y. G. Guo, *Adv. Mater.* **2018**, *30*, 1803765.
- [26] X. Xu, R. Zhao, W. Ai, B. Chen, H. Du, L. Wu, H. Zhang, W. Huang, T. Yu, *Adv. Mater.* **2018**, *30*, 1800658.
- [27] Y. Xiao, D. Su, X. Wang, S. Wu, L. Zhou, Y. Shi, S. Fang, H. M. Cheng, F. Li, *Adv. Energy Mater.* **2018**, *8*, 1800930.
- [28] B. Chen, Y. Meng, F. Xie, F. He, C. He, K. Davey, N. Zhao, S. Z. Qiao, *Adv. Mater.* **2018**, *30*, 1804116.
- [29] J. Liang, X. Y. Yu, H. Zhou, H. B. Wu, S. Ding, X. W. Lou, *Angew. Chem., Int. Ed.* **2014**, *53*, 12803.
- [30] B. Y. Guan, L. Yu, X. W. Lou, *J. Am. Chem. Soc.* **2016**, *138*, 11306.
- [31] X. Zhao, J. Wang, R. Yu, D. Wang, *J. Am. Chem. Soc.* **2018**, *140*, 17114.
- [32] J. Zhang, J. Wan, J. Wang, H. Ren, R. Yu, L. Gu, Y. Liu, S. Feng, D. Wang, *Angew. Chem., Int. Ed.* **2019**, *58*, 5266.
- [33] J. Liang, H. Hu, H. Park, C. Xiao, S. Ding, U. Paik, X. W. Lou, *Energy Environ. Sci.* **2015**, *8*, 1707.
- [34] F. Pei, T. An, J. Zang, X. Zhao, X. Fang, M. Zheng, Q. Dong, N. Zheng, *Adv. Energy Mater.* **2016**, *6*, 1502539.
- [35] Y. Zhang, Z. Ding, C. W. Foster, C. E. Banks, X. Qiu, X. Ji, *Adv. Funct. Mater.* **2017**, *27*, 1700856.
- [36] Y. Zhang, C. W. Foster, C. E. Banks, L. Shao, H. Hou, G. Zou, J. Chen, Z. Huang, X. Ji, *Adv. Mater.* **2016**, *28*, 9391.
- [37] B. Li, B. Xi, F. Wu, H. Mao, J. Liu, J. Feng, S. Xiong, *Adv. Energy Mater.* **2018**, *30*, 1803070.
- [38] Y. Wu, Y. Jiang, J. Shi, L. Gu, Y. Yu, *Small* **2017**, *13*, 1700129.
- [39] J. Y. Hwang, H. L. Du, B. N. Yun, M. G. Jeong, J. S. Kim, H. Kim, H. G. Jung, Y. K. Sun, *ACS Energy Lett.* **2019**, *4*, 494.
- [40] M. Zhou, Y. Xu, C. Wang, Q. Li, J. Xiang, L. Liang, M. Wu, H. Zhao, Y. Lei, *Nano Energy* **2017**, *31*, 514.
- [41] X. Yang, C. Wang, Y. Yang, Y. Zhang, X. Jia, J. Chen, X. Ji, *J. Mater. Chem. A* **2015**, *3*, 8800.
- [42] M. Zhou, Y. Xu, J. Xiang, C. Wang, L. Liang, L. Wen, Y. Fang, Y. Mi, Y. Lei, *Adv. Energy Mater.* **2016**, *6*, 1600448.
- [43] X. W. Lou, L. A. Archer, Z. Yang, *Adv. Mater.* **2008**, *20*, 3987.
- [44] F. Holtstiege, P. Bärman, R. Nölle, M. Winter, T. Placke, *Batteries* **2018**, *4*, 4.